Emission imaging and CFD simulation of a coaxial single-element GOX/GCH_4 rocket combustor

Fernanda F. Winter*, Nikolaos Perakis† and Oskar J. Haidn‡
Chair of Turbomachinery and Flight Propulsion, Technical University of Munich, Boltzmannstr. 15, 85748 Garching, Germany

The present study aims to contribute to the understanding of the thermal behavior and mixing processes of GOX/GCH_4 single element shear coaxial injector, to provide sufficient data for the validation of numerical tools. Standard experimental measurements as well as optical diagnostic through emission analysis provide detailed information about the heat flux at the hot inner walls of the combustion chamber and flame structure for a pressure level of 10 and 20 bar with O/F variation between 2.6 and 3.4. A RANS simulation of the combustion and wall heat transfer in the combustor was carried out using a Flamelet model. The numerical results show a satisfying agreement with the experiment and are able to capture the effects of varying O/F on heat flux distribution and OH mass fraction.

Nomenclature

B/W	=	black and white
$CMOS$	=	complementary metal-oxide semiconductor
GOX	=	gaseous oxygen
$GCH4$	=	gaseous methane
$iCCD$	=	intensified CCD
LOX	=	liquid oxygen
NL	=	natural
OH^*	=	hydroxyl radicals
O/F	=	oxidizer to fuel ratio
VR	=	velocity ratio
d	=	diameter
J	=	momentum flux ratio
$\dot{m}$	=	mass flow rate
P	=	pressure
$\dot{q}$	=	heat flux
t	=	time
T	=	temperature
v	=	velocity
θ	=	angle
ρ	=	density

subscripts

cc	=	combustion chamber
i	=	internal
m	=	methane
o	=	oxygen
t	=	total
win	=	additional

*M.Sc., Technical University of Munich, fernanda.winter@ltf.mw.tum.de.
†M.Sc., Technical University of Munich
‡Prof. Dr.-Ing., Technical University of Munich

I. Introduction

Many papers were published in the past years addressing the merits of methane as a propellant candidate. In fact, the propellant combination LOX/methane is a good propellant alternative to the current LOX/hydrogen thrust engines due to its higher density, expected good performance when compared to other hydrocarbons, good cooling capability, low soot production, and low-cost handling [1], [2], [3], [4].

Although many studies have already been performed [5], [6], [7], the development and optimization of a liquid rocket engine for a new propellant combination demand not only detailed understanding of all physical phenomena that determine performance but also validation of numerical tools.

Under these circumstances and considering that the currently established engine concepts depend on a certain number of assumptions due to missing experimental and analytical database, and considering that there is still insufficient knowledge about performance and heat release for this propellant pair, the Technical University of Munich has experimentally and numerically investigated the combustion process and heat transfer of rocket combustion chambers. All combustors, which are tested at the Chair of Turbomachinery and Flight Propulsion (LTF) operate with gaseous oxygen and gaseous methane in the context of the national research program Transregio SFB/TRR-40 on "Technological Foundations for the Design of Thermally and Mechanically Highly Loaded Components of Future Space Transportation Systems".

Currently the group operates four principally different GOX/GCH_4 combustion chambers, all of which have the following characteristic features in common: ambient temperature gaseous propellants, identical shear coaxial injectors, identical injector/wall distances and an identical contraction ratio which guarantees an identical Mach number of 0.25. Two combustion chambers are operated with a single injector element but have different chamber cross sections, square and circular, in order to enable the studies on flame stabilization and heat transfer.

The square cross section combustion chamber has been used as a validation test case for numerical simulations. The test load point selected was 20 bar pressure and a mixture ratio of 2.6. For this mixture ratio, methane is injected faster than the oxygen jet located in the central part of the injector. This effect has an impact on the corner vortices due to the combustion chamber's rectangular cross section.

Different numerical tools and approaches have been applied to this load point in an international cooperation group composed of CERFACS, ArianeGroup (formerly ADS), JAXA, IVLR of the University of Stuttgart, UniBW and the chairs of Thermodynamics and Flight Propulsion of the Technical University of Munich. The results have clearly shown significant differences in their capability to reproduce the experimental heat flux. Although most of the predictions obtain a similar maximum temperature inside the combustion chamber, the predicted flame shapes are different. In general, the predictions vary notably [8].

In order to improve the understanding of the obtained experimental results and to reduce the discrepancies between experimental and numerical results, an optical window has been implemented in the combustion chamber enabling the analyses of test results through optical diagnostics in addition to the classical measurement techniques such as pressure and wall temperature measurements. The optically accessible combustion chamber allows the determination of the flame spreading angle and recirculation length – information which might be relevant for the improvement of numerical tools.

In this context, the present work is performed as a complementation of previous investigations performed on heat transfer [9] and injector-injector/injector-wall interaction [10]. The tests are performed at 10 and 20 bar pressure level with mixture ratio variation between 2.6 and 3.4. The images obtained with an iCCD camera are used to illustrate not only the global flame structure but also the flame front in the near injector zone.

II. Hardware description

The square cross section combustion chamber previously mentioned and used for this investigation is modular and consists of 2 segments, a long and a short one, for an overall length of 290 mm. The combustion chamber is capacitively cooled and has a square cross section of 12 mm x 12 mm. It operates with gaseous oxygen and methane as propellants. The material selected for the combustion chamber and nozzle segments is oxygen-free copper (Cu-HCP) due to its high thermal conductivity. The nozzle segment has a rectangular cross section of 4.8 mm x 12 mm. Tab. 1 summarizes the internal combustion chamber dimensions.

The injector head is designed to allow different injector configurations. For the current study, a shear coaxial element is integrated as shown in Fig. 1. The injector element comprises a 4 mm diameter gap for the central oxygen jet and a 0.5 mm annular gap for methane. Tab. 2 presents the injector's main characteristic dimensions. For simplicity, the GOX post is mounted flush with respect to the faceplate and no tapering is applied. In order to provide homogeneous inflow

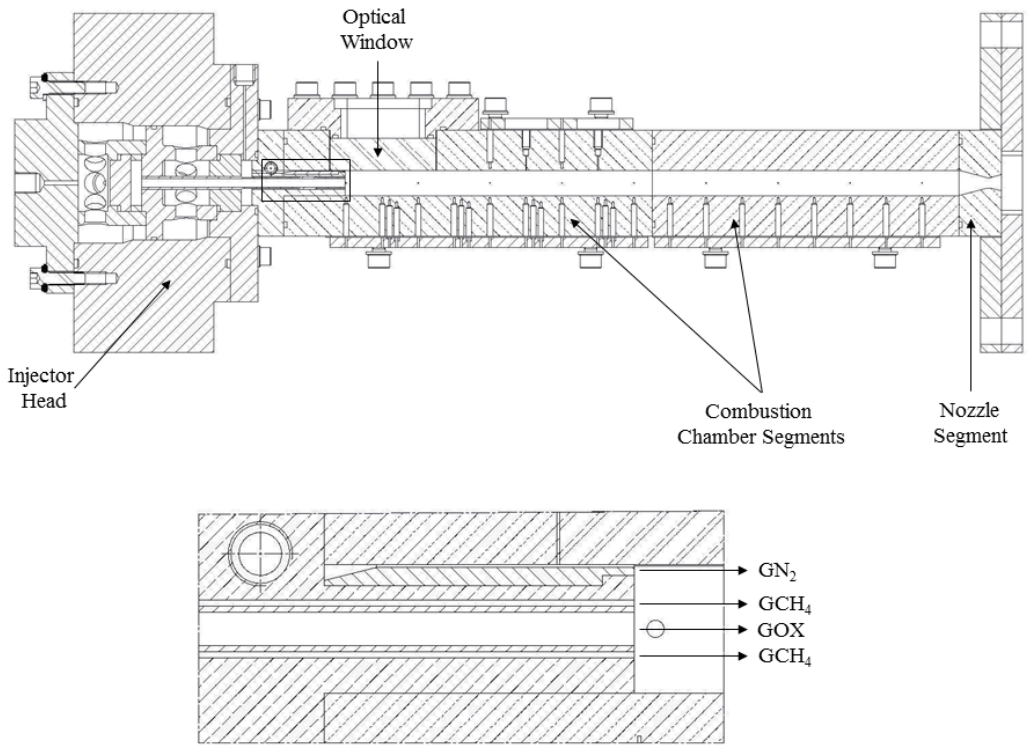

Fig. 1 Setup and injector configuration.

conditions, the injector is equipped with porous inserts in the oxygen and methane manifolds.

The combustion chamber is equipped with equally spaced pressure transducers and thermocouples type T spring-mounted in the wall along the chamber axis to characterize the combustion process and to monitor heat release. WIKA A10 pressure transducers are used to record the evolution of the static wall pressure and are individually calibrated before the test campaign. The spring loading of the thermocouples provides a constant force to ensure continuous contact between the thermocouple's tip and the base of the hole. This thermocouple mounting configuration aims to minimize the chance of potential loss of contact caused by thermal expansion or vibrations during the test. More detailed information, such as the thermocouple positions and distances from the hot gas side can be found in [11].

Table 1 Combustion chamber geometry

Length	290	[mm]
Width	12	[mm]
Height	12	[mm]
Throat height	4.8	[mm]
Contraction ratio	2.5	[-]

Table 2 Injector geometry

GOX inner diameter	4	[mm]
GOX post wall thickness	0.5	[mm]
GCH_4 external diameter	6	[mm]
Injector area ratio	0.7	[-]

The first segment of the combustion chamber is also equipped with a quartz optical window, which allows optical access to the flame interaction in the near injector area. The flat window in combination with the rectangular cross section of the hardware has the advantage that it avoids certain unwanted effects, such as flow disturbances, which are caused by the presence of window corners and usually occur when a flat window is mounted in a round combustion chamber.

A film cooling system using gaseous nitrogen as coolant is used to protect the optical window from the heat loads of the combustion and soot deposition. A sensitivity analysis was performed in regard to the influence of film cooling in the near injector area, which is the area of interest for optical diagnostics, and on the stability of the flame. According to the test results, no significant difference was observed in the temperature profiles and heat fluxes obtained. Considering,

in addition to the sensitivity analysis results, that the film cooling mass flow is about 1g/s for the 10bar cases and 2g/s for the 20 bar cases, which is about 3% of the total mass flow rate, and a non-reactant coolant is used, the near injector flow phenomena are not influenced.

III. Operating conditions

A spark torch igniter is used to ignite the propellant mixture. The igniter operates with gaseous methane and oxygen and is located in the middle of the combustion chamber with respect to the axial direction. Propellants, purge gas and film cooling mass flow rates can be adjusted by adapting the upstream pressure of sonic measuring orifices located in the feedlines. For determination of the load points, the characteristic velocity is calculated with the software tool NASA CEA2 and combustion efficiency is assumed to be equal to 1.

To operate the combustion chamber, a test sequence is programmed into the control system. As already described and explained in detail in [10], [12], the sequence is divided into three main periods: transient start-up with ignition, main combustion chamber operation and shut down. The igniter operates for 300 ms to ensure ignition of the combustion chamber for a total burning time of 3 s. After successful ignition of the main combustion chamber the igniter is switched off. The same sequence is applied to all tests performed.

A test campaign was performed at 10 and 20 bar pressure nominal level with O/F variation between 2.6 and 3.4 with film cooling percentage of about 3% with respect to the total mass flow rate. Each operating point is run at least two times to check the repeatability of the recorded test data. Fig. 2 und Fig. 3 show the test operation conditions and resulting velocity ratio and momentum flux ratio. Full and empty markers stand for 20 and 10 bar nominal pressure, respectively.

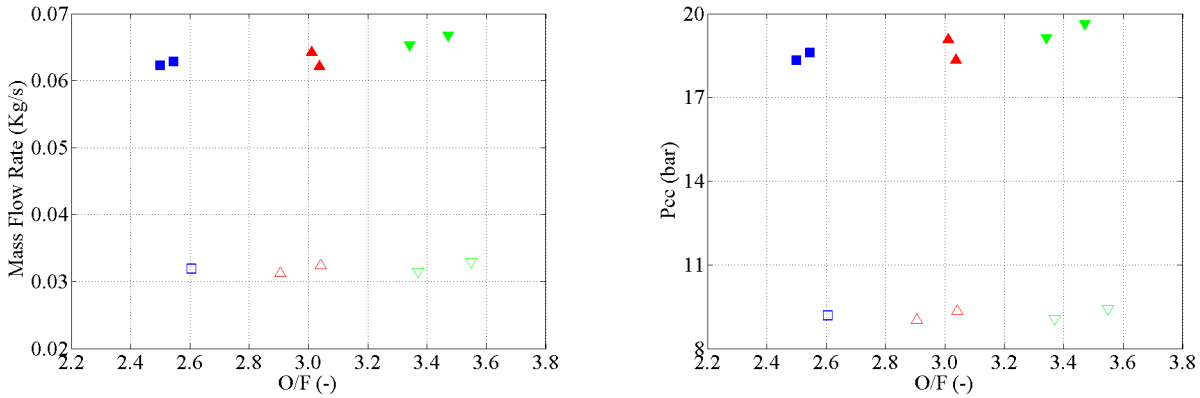

Fig. 2 Operated test conditions (left) and mean combustion chamber pressure (right).

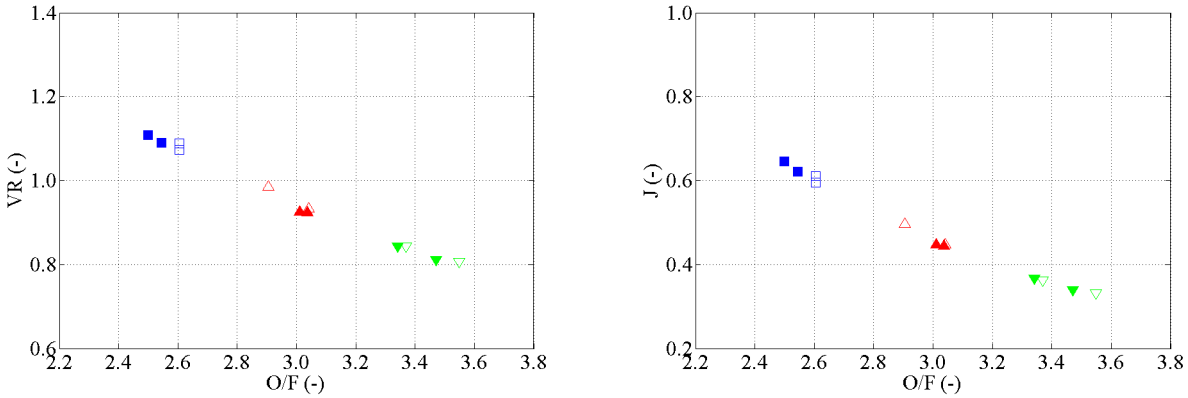

Fig. 3 Test resulting velocity ratio (left) and momentum flux ratio (right).

IV. Optical diagnostic and image post-processing

To detect spontaneous emission of intermittently existing hydroxyl (OH^*) radicals it is necessary to use a relevant narrow band-pass filter (308 ± 5 nm), which highly decreases the light signal that reaches the camera sensor. Therefore, the intensified CCD camera Flame Star 2 was used. The camera system is equipped with a 12 bit sensor, an appropriate UV image intensifier, and a fixed focal length 105 mm 1:4.5 Nikon Nikkor UV lens. The near-injector area is visualized with a resolution of 384 x 256 pixels. To obtain nearly instantaneous images, a short exposure time is desirable. With the image intensifier used within this investigation, an exposure time of 5µs was used. No external lighting was applied.

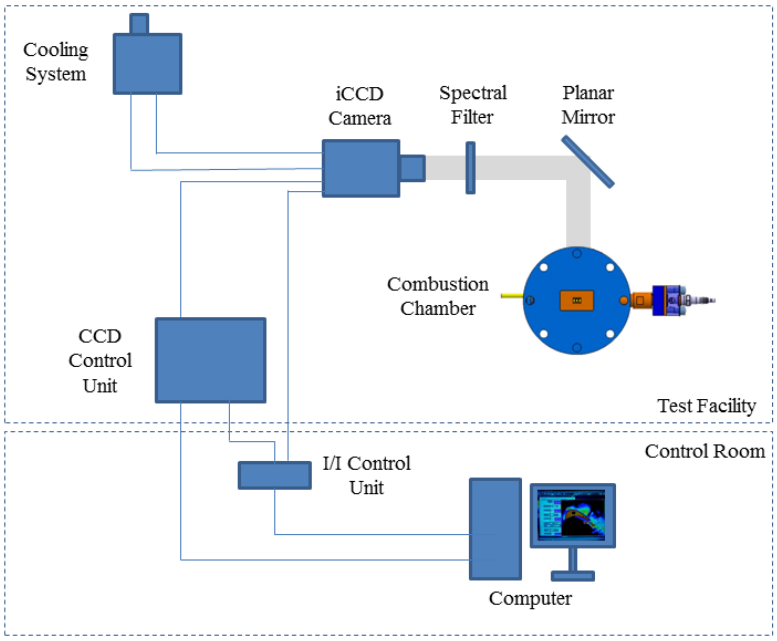

Fig. 4 Optical setup for hydroxyl emission imaging.

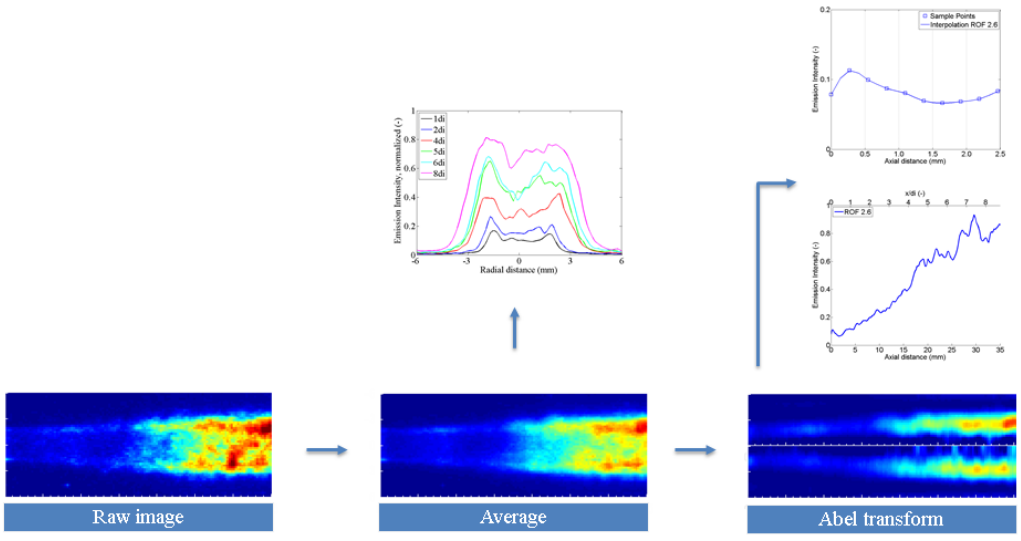

Fig. 5 Image post-processing steps.

A schematic of the optical setup is shown is Fig. 4. The camera was positioned on an optical bench located next to the test bench and the image of the combustion chamber was reflected into the camera sensor with a planar mirror, which was positioned above the optical window with a 45-degree angle. The camera cooling system enables a constant temperature in the camera sensor reducing therefore measurement erros related to temperature variations. In order to obtain the same optical resolution for all loadpoints the camera was positioned at the same distance from the combustion chamber for all tests.

The recorded images were post-processed using image processing techniques. The consecutive instantaneous images were averaged in the phase of stable combustion operation at the evaluation time and an inverse Abel transformation was applied to the image obtained. This step was required in order to compare the experimental results with numerical simulations and specially for the near injector field to determine the dimentions of the reaction zone between oxygen and methane. Fig. 5 summarizes and illustrates the image post-processing steps. After the post-processing radial and axial profiles of the flame were plotted from the average and resultant Abel transform images, respectivelly.

V. Experimental Results

The main goal of this investigation is to profit from the experimental results obtained through emission imaging in addition to the results obtained with standard measurement techniques, in order to fulfill the lack of understanding of methane/oxygen combustion process and heat transfer, and therefore help to improve numerical models.

Due to the fact that the combustion chamber is capacitively cooled and the test time is limited to 3 s, thermal steady state conditions are not reached. In this way, a representative time interval, which is at 2/3 of the burning time, was selected for the data evaluation as a characteristic hot run time step.

A. Near injector flame shape

Typical normalized averaged OH^* emission images recorded in the interval of the evaluation time for the tests performed at 20 bar pressure level and their corresponding radial profiles for different axial positions are shown in Fig. 6. From the top to the bottom the results of each mixture ratio are displayed in progressive order. The flow direction is from left to right and the visualization area corresponds to 12 x 35 mm^2 .

All image intensities habe been normalized to cover the full color scale. The normalization has been performed with the maximum emission intensity of all tests at 20 bar pressure level, so that the tests within different mixture ratios can be compared.

For all tests performed in this investigation, the flame envelops the oxygen jet assuming a cylindrical shape. After a certain axial distance, the flame expands radially. The flame continues to expand for some millimeters of the visible optical access until it starts to assume a cylindrical shape again.

It can be seen from these images that an increasing methane injection velocity (and, thus, increasing velocity ratio and momentum flux ratio) leads to a constriction of the flame and therefore of the total flame volume within the optically accessible area. The flame volume reduction can be well observed in the corresponding radial profile for the different axial positions, see Fig. 6 right side.

This effect, which is visible during both operating pressure tests, is explained by the fact that in this case the methane jet is faster than the internal oxygen jet. This means that the inner oxidizer flow is pulled outward and the distance between flame front and combustion chamber wall becomes smaller.

For the higher mixture ratio case, for which the annular methane jet is pulled inward by the faster oxygen jet due to shear forces, flame fluctuations are mainly predominated in the shear layer between the propellants increasing therefore the distance of the flame front to the combustion chamber wall.

B. Reaction zone and flame anchoring

The experimental images are taken from the side of the flame, thus showing the line-of-sight integrated emission. The mole fraction of hydroxyl in the combustion of hydrocarbons is generally low, therefore self-absorption is often insignificant, especially for low-pressure cases. In this way the reconstruction of a two-dimensional radial distribution from measured projections or line integrals can be obtained by the application of an inverse Abel transform. This data gives a beter insight into the reaction zone in the direct vicinity of the injector region and can directly be compared to radiation models applied to the axis-symmetric simulation domain, which was also the objective of this study.

With this purpuse, the time-averaged OH^* emission images from section A have been de-convoluted using the Abel transformation. The code for calculation of the deconvolution uses the Fourier method [13]. This method is used

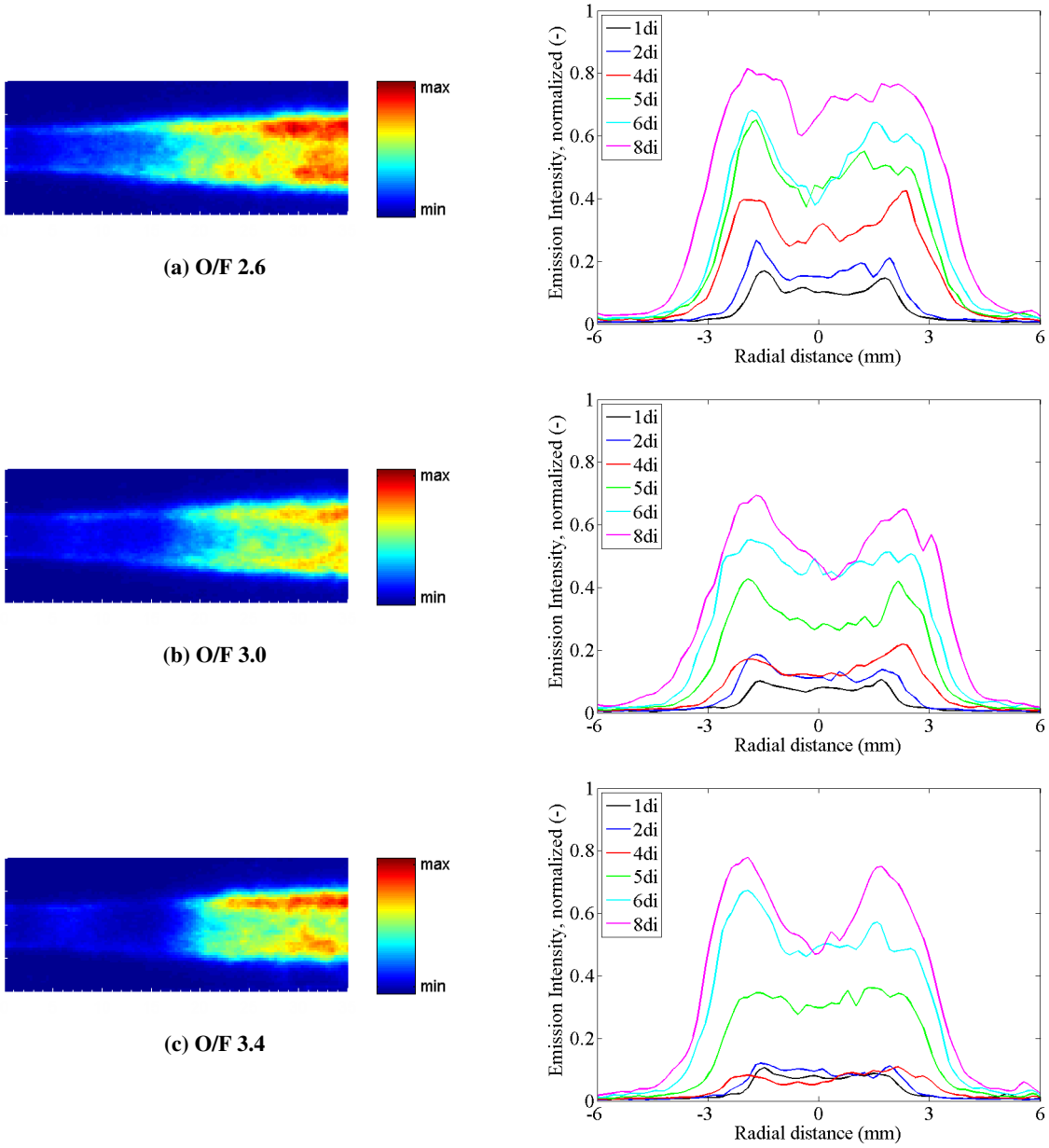

Fig. 6 Average (right) and radial profile (left) emission intensity for an axial distance of 1, 2, 4, 5, 6 and 8 times the injector inner diameter for the mixture ratios 2.6, 3.0 and 3.4 at 20 bar pressure.

because neither noise smooting nor any other kind of pre-treatment of the measured data is necessary.

Furthermore, the requirements for the application of the Abel transform with respect to the light rays are that the lines of sight are single, non interfering lines, forming a parallel projection of the object under investigation, which was acomplished by the use of an lens aperture of F22.

The resulting images from the de-convolution are shown in Fig. 7. From the top to the bottom the images are sorted by mixture ratio, from 2.6 to 3.4, and the flow direction is from left to right. The images have been normalized as in section A.

The Abel transform can be used to estimate the dimenson of the reacting shear layer between gaseous oxygen and methane. It can be seen in Fig. 7 that generally the shear layer grows continuosly with increasing axial distance after about 20 mm from the injection plane.

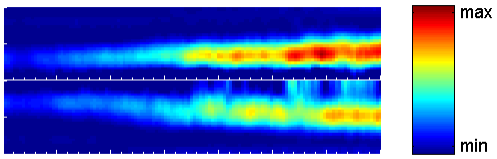

(a) O/F 2.6

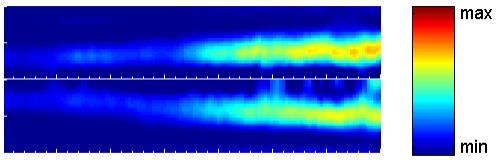

(b) O/F 3.0

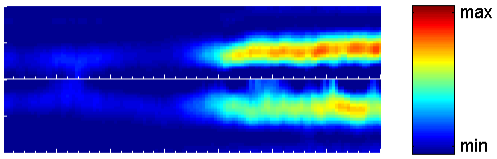

(c) O/F 3.4

Fig. 7 Abel transformed intenisity for the mixture ratio 2.6, 3.0 and 3.4 tests at 20 bar pressure.

For the case with lower mixture ratio, the reacting shear layer between gaseous oxygen and methane is thicker. Velocity ratio and momentum flux ratio, clearly influence the near injector precesses. Increasing the injection velocity ratio and the momentum flux ratio (at constant chamber pressure) increases the overall averaged emission intensity in the near injector field of interest. For the O/F 3.0, for which velocity ratio is nearly one, shear forces are weaker and therefore the shear layer grows more slowly.

Since the flame shape appears symmetrical in the axial direction but brighter in the top part when comparing to the bottom, the axial profile of the maximum emission intensity for the upper and lowler part of the flame of all three mixture ratio cases has been plotted in Fig. 8 in order to provide an overview of their differences. The profiles have the same qualitative trend. The emission intensity difference of approximatelly 10% is due to a non perfect concentricity of the coaxial injector.

By comparing the axial profiles for the different mixture ratios still in Fig. 8, it can be seen that emission intensity is higher for lower mixture ratios until an axial position of about 20 mm or five times the injector internal diameter, di. Then the emission intensity for mixture ratio 3.4 increases progressively until the end of the optically accessible field of view.

Between 5 and 10 mm an elevation in the axial profile of maximum emission intensity is observed. This elevation is influenced by the mixture ratio and is most likely to be caused by a recirculation zone.

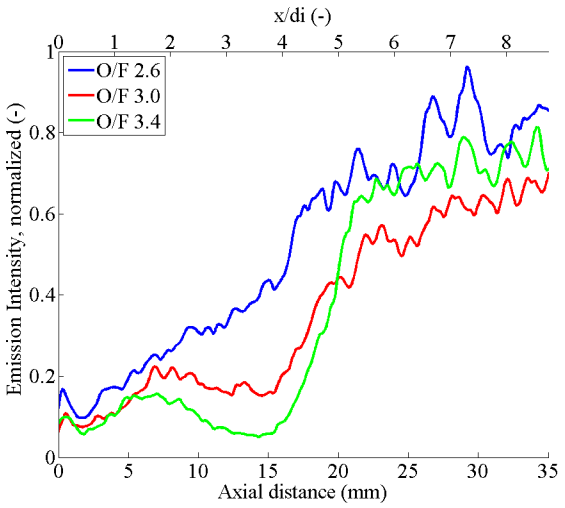

(a) Flame top

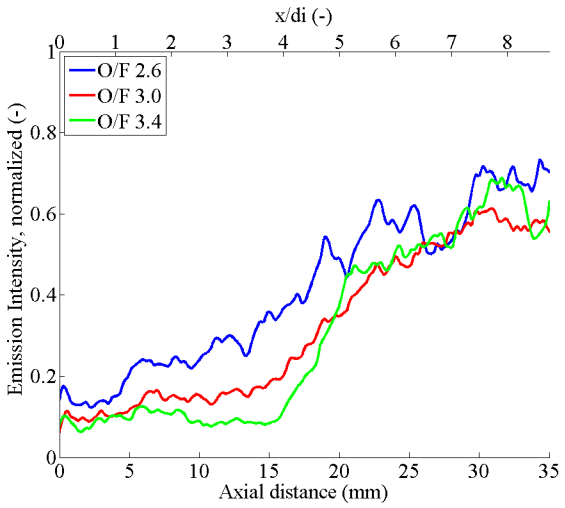

(b) Flame bottom

Fig. 8 Axial profile of the line of maximum intensity of the Abel transform for the top and bottom part of the flame for O/F 2.6, 3.0 and 3.4 at 20 bar pressure.

Former test campaigns with this combustion chamber have found traces of soot deposition in this specific region in a circular shape, which is typical for a recirculation zone. For lower O/F cases the elevation tends to disappear and the emission intensity tends to increase in a uniform and progressive way.

It can also be assumed from the images of Fig. 7 that the flame anchors in the wake of the GOX post tip in all test cases. Previous studies [14], [15], [16] have already determined that as the flow passes a step, it separates and a shear layer develops, providing a low-velocity zone for the flame to reside and propagate into the reactant flow.

This recirculation zone behind the step supplies combustion radicals with enough energy to overcome the activation energy of incoming reactants, thus initiating burning within the shear layer. Fig. 9 shows the axial profile of maximum emission intensity for the top and bottom part of the flame of all three mixture ratio cases for the first 2.5 mm of the optial view field. The anchoring point is clear to be seen as an elevation in the axial profile in the first millimeter. The anchoring position and the intensity is dependent on the mixture ratio. For the case of O/F 3.0 it is shifted to a more downstream position and for the case of O/F 3.4 is not well defined, having a flatter pattern.

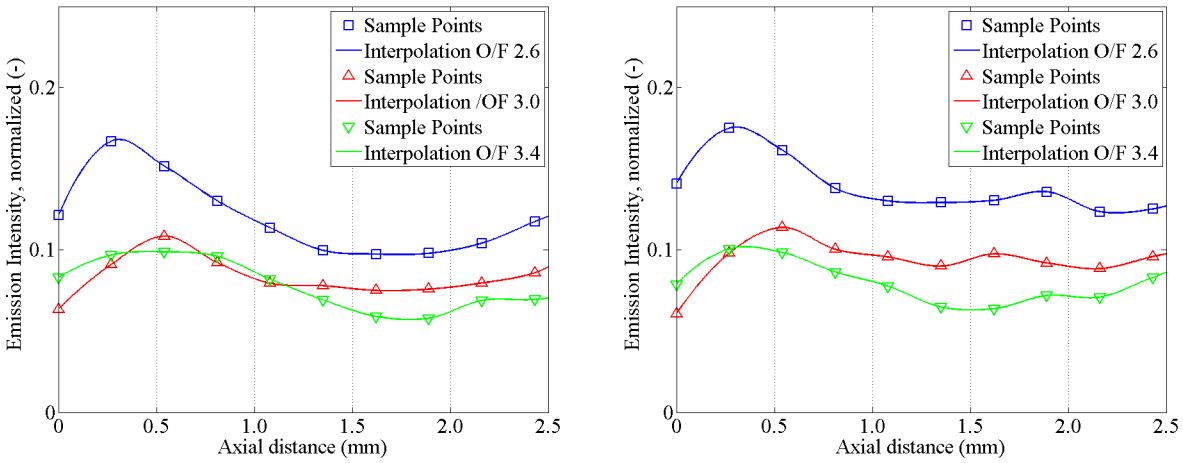

(a) Flame top **(b) Flame bottom**

Fig. 9 Axial profile of the line of maximum intensity of the Abel transform for the top and bottom part of the flame for O/F 2.6, 3.0 and 3.4 at 20 bar pressure for the first 2.5 mm of the optical view field.

C. Pressure Influence

The test campaign was also performed at the nominal pressure level of 10 bar. The same results as for the tests performed at 20 bar were encountered for the tests performed at 10 bar pressure with respect to the flame shape, reaction zone and flame anchoring. Therefore this subchapter will discuss only the pressure influence on the emission intensity measured.

In order to compare the test results at two different pressure levels, the time-averaged images were normalized with the maximum measured emission intensity of all test cases at 20 bar pressure level. Fig. 10 shows the axial profile of the maximum intensity for the mixture ratios 2.6, 3.0 and 3.4 at 10 and 20 bar and Fig. 11 shows the total averaged emission intensity for the three mixture ratios as a function of the mean combustion chamber pressure.

It is evident from Fig. 10 and Fig. 11 that the total flame emission intensity decreases with decreasing combustion chamber pressure. With the reduction of the combustion chamber pressure from 20 to 10 bar, the averaged emission intensity drops by about 60%.

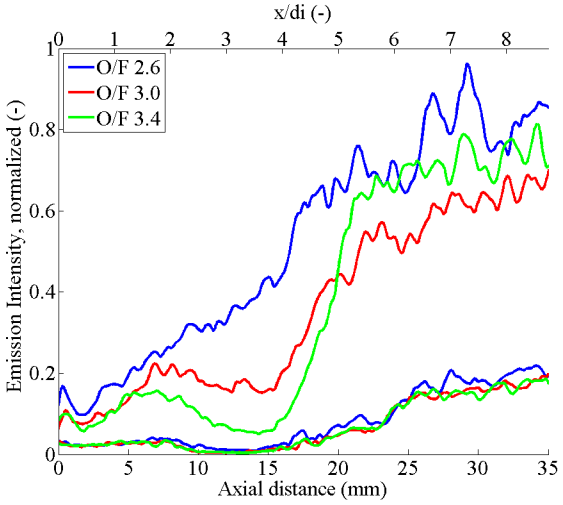

Fig. 10 Axial profile of the maximum intensity of the Abel transform for the top part of the flame for O/F 2.6, 3.0 and 3.4 at 10 and 20 bar pressure.

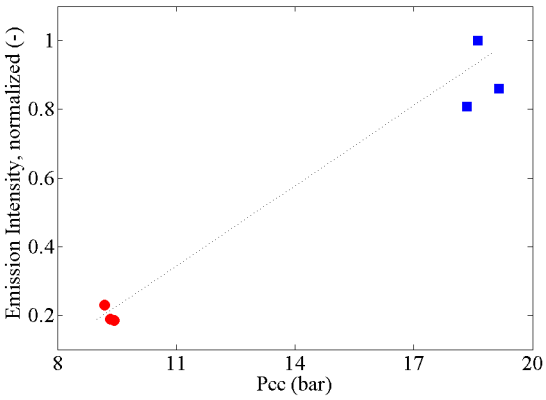

Fig. 11 Averaged emission intensity of O/F 2.6, 3.0 and 3.4 as a function of the mean combustion chamber pressure.

VI. Numerical Simulation

A. Computational setup

For the comparison with the experimental data, a CFD simulation was carried out. The 3D Reynolds-averaged Navier Stokes equations (RANS) are solved using a finite volume method with the commercial code ANSYS Fluent [17]. To take advantage of the geometrical symmetry of the single element rocket combustor, only one fourth of the chamber domain is modeled. The mesh resulting from a grid study consists of approximately 1.8 million cells and is shown in Fig. 12. The wall mesh resolution is chosen as to satisfy the $y^+ \approx 1$ condition. The red annulus corresponds to the fuel massflow inlet, whereas the blue area shows the oxygen massflow inlet.

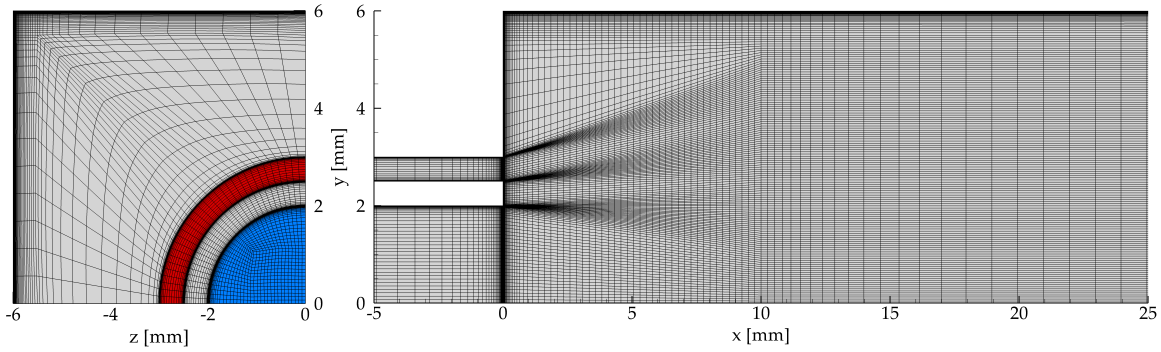

Fig. 12 Mesh at faceplate, massflow inlets and symmetry plane.

For the injection temperature, the measured temperatures of the gases are defined at the boundary. At the xy and xz planes, a symmetry boundary condition is imposed and the mesh in the first 25 mm of the chamber can be seen in Fig. 12. For the thrust chamber walls, a no-slip condition is fullfilled and a temperature profile is prescribed. This was obtained using the thermocouple measurements at the dedicated positions 1mm away from the hot gas wall and was

evaluated using an inverse heat transfer method as described by Celano et al. [18] and Perakis et al. [19]. Finally for the nozzle outlet a pressure boundary condition is defined and all remaining walls are adiabatic and have a no-slip condition.

The adiabatic Flamelet model described by Peters [20] is implemented in this combustion simulation. The tabulation of species mass fractions and temperature occurs using the mixture fraction $\tilde{Z}$, the mixture fraction variance $\tilde{Z''^2}$ and the scalar dissipation rate $\tilde{\chi}$. A β-PPDF is used for the turbulence/chemistry interaction. The chemical reaction mechanism used for the generation of the Flamelet tables is the one from Slavinskaya et al. [21]. For the turbulence model, the standard $k-\epsilon$ was utilized, using a two-layer model by Wolfshtein [22] for the wall treatment, since it was shown to deliver better results when combined with the Flamelet model compared to other RANS turbulence models [23]. For the closure of the turbulent flux terms the turbulent Prandtl/Schmidt number combination of 0.9/0.6 is chosen. The molecular properties of the gas are calculated by means of the kinetic theory [24] and the thermodynamic properties using NASA polynomials.

B. Temperature and heat flux distribution

To analyze the effect of O/F on the heat loads and flame structure, CFD simulations were performed for O/F = 2.2, 2.6, 3.0 and 3.4 at 20 bar nominal pressure. The temperature distribution on the symmetry plane along with the stoichiometric line resulting from the CFD are shown in Fig. 13 for the different load points.

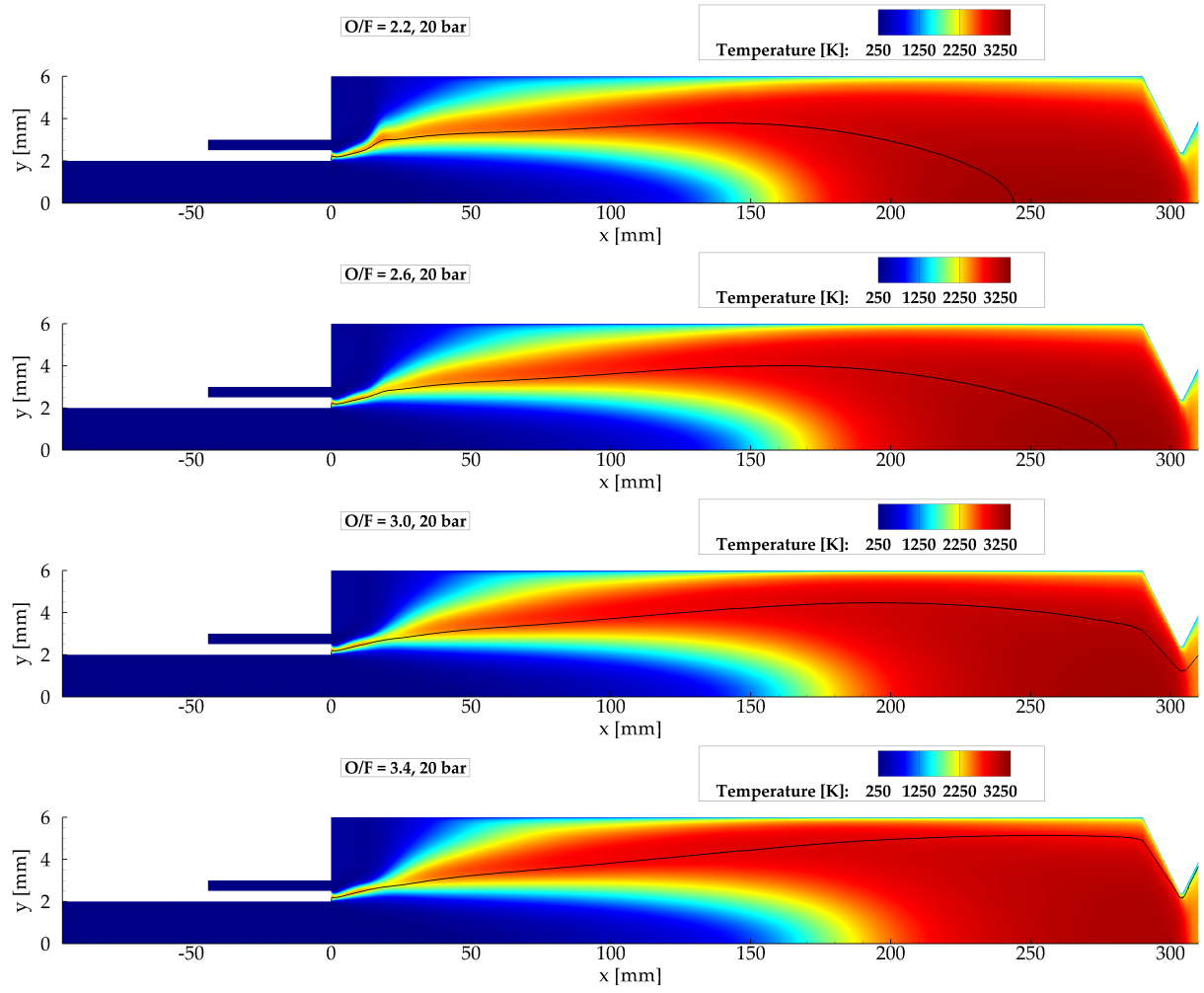

Fig. 13 Temperature field in the symmetry plane. The solid black line shows the stoichiometric concentration.

It is evident that the mixture fraction has a large influence on the length of the flame for the single element combustor.

Specifically, the increasing O/F appears to shift the flame further downstream up to the point where the flame (here characterized by the position of the stoichiometric line) exits the chamber leading to an incomplete combustion.

This effect can be understood when examining the velocity ratio and momentum flux ratio of the load points. In all of the cases, the velocity ratio (v_{CH_4}/v_{O_2}) is between 1.35 and 0.85, namely very close to unity. The momentum flux ratio however ($\rho_{CH_4}v_{CH_4}^2/\rho_{O_2}v_{O_2}^2$) steadily decreases with higher O/F, due to the increased oxygen velocity, as shown in Fig. 3. For O/F=2.2 it is equal to 0.90, whereas for the O/F=3.4 case it reaches a value of 0.37. The higher momentum of oxygen pushes the mixing region further downstream and leads to this observed shift of the flame to positions closer to the nozzle.

This observed shift of the flame downstream is also confirmed by examining the heat flux profile directly at the wall. Figure 14 shows the experimentally evaluated heat flux along with the numerical result from the CFD. The heat flux profile was obtained using the in-house inverse heat conduction code Ro$\dot{q}$FITT (Rocket $\dot{q}$ Flux Inverse Thermal Tool) [19] under the assumption that the heat flux profile at each axial position is constant along the circumferential direction.

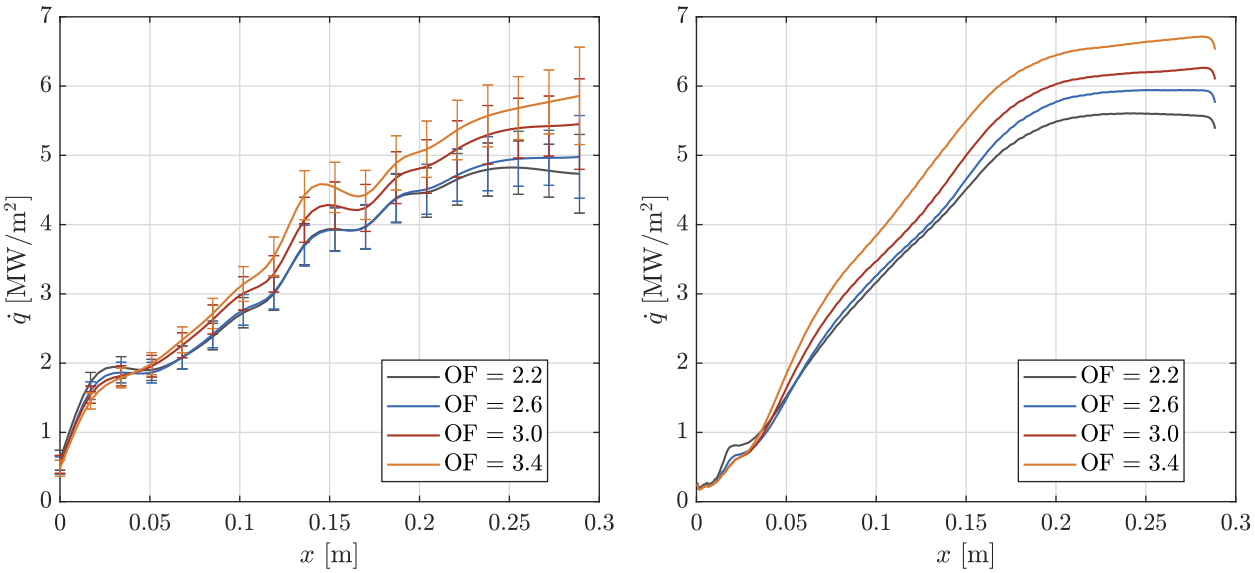

Fig. 14 Heat flux profile from the experiment (left) and the CFD simulation (right).

The depicted CFD results correspond to the average heat flux value for each axial position. Both the experimental and numerical profiles show an identical qualitative trend. Specifically, it is shown that with increasing O/F, the absolute heat flux level is increased and the maximum of the heat flux value travels further downstream. The first effect is due to the higher heat release and flow temperature in higher O/F conditions, since the global mixture ratio in the chamber is closer to stoichiometry. Regarding the second point, the heat flux maximum in the chamber indicates the end of energy release and hence the end of combustion. For positions further downstream, there is not significant energy release and the heat flux is reduced because of the thermal boundary layer increase. For the operating points with O/F=3.0 and O/F=3.4, no heat flux maximum is observed (heat flux is steadily increasing), hinting that the combustion is not complete in the combustion chamber. This agrees very well with the flame image illustrated in Fig. 13.

Compared to the experiment, the CFD tends to predict a higher average heat flux. This can be attributed both to the experimental evaluation error as well as the numerical models used in the simulation. Regarding the inverse method for the experimental evaluation, the assumption of constant heat flux even at the corners of the cross section is questionable. A study was carried out during this work, where different profiles were assumed for the heat flux along y and z (e.g. parabolic profile) but it was shown that the average value of the heat flux for each axial position is insensitive to the assumed profile. Regarding the CFD, the use of an eddy-viscosity model for the turbulence (standard $k-\epsilon$) implies that the secondary flows at the corners and recirculation zone are not captured adequately. Although these effects are less prominent in cylindrical chambers, they can have a significant effect in a rectangular configuration like this one.

Despite these known issues, the CFD is able to capture not only the increasing heat flux level and shift of heat flux maximum towards the exit of the chamber but also the qualitative trend close to the faceplate. For axial positions shorter than 40mm for the injection plane, the smaller O/F load points appear to have a higher heat flux both in the

experiment and the CFD. This can be attributed to the higher methane velocity at those conditions, which leads to a higher expansion angle of the jet and therefore to a shorter distance between the flame and the wall.

VII. Comparison of OH* emission measurement with numerical results

For the comparison of the OH* emissions from the experiment with the numerical results, several methods have been proposed. Often in literature the OH concentrations (which are available from the combustion simulation) are assumed to be identical to the OH* concentrations and are directly compared to the measured intensities.

Fiala et al. [25] proposed an a posteriori calculation method of the OH* concentration using the assumption of thermal equilibrium. However this method does not account for turbulent fluctuations of the temperature and OH field and is only valid for laminar combustion. When applied to turbulent combustion applications, it tends to underpredict the width of the OH* zone and hence also the flame thickness. For that reason for the present comparison the OH mass fraction is taken for the comparison with the experiment.

All emission intensities of the experimental images and OH mass fractions of the numerical simulations have been normalized to cover the same full color scale. The normalization has been performed with the maximum emission intensity of all tests for the experimental images and with the maximum OH mass fraction of all cases of the numerical simulation. This way both, experimental and numerical images, have been normalized in the same way and the tests within different mixture ratios can be compared.

Fig. 15 presents the experimental and numerical results for the mixture ratios 2.6, 3.0 and 3.4 at 20 bar pressure.

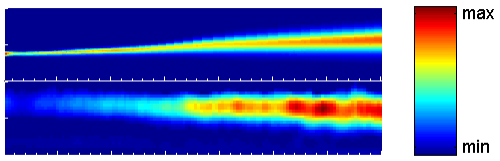

(a) O/F 2.6

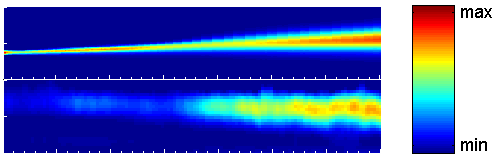

(b) O/F 3.0

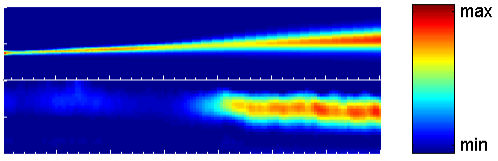

(c) O/F 3.4

Fig. 15 Numerical and experimental results for the mixture ratios 2.6, 3.0 and 3.4 at 20 bar pressure.

The simulation captures very accurately the position, in which the flame expands radially for each different O/F. This is clearly seen in Fig. 16, which shows the axial profiles of the line of maximum intensity (experiment) and mass fraction (numerical) for the O/Fs 2.6, 3.0 and 3.4. The plots with dashed lines correspond to the experimental results and with solid lines to the results of the numerical simulations.

Like in the experimental results, the reacting shear layer between gaseous oxygen and methane obtained from the simulations grows continuosly with increasing distance from the injection plane after about half of the optically accessible window length. A pick in the profile obtained from the numerical simulation is observed in the first 0.5 mm, which corresponds to the anchoring position. The same is observed in the profile of the experimental results but the intensity of the pick is not as high as from the numerical simulation. At about 10 mm in the profile of the OH mass fraction an elevation is to be seen, which is also present in the profile of OH* emission intensity. This elevation is most likely to be caused by the recirculation zone as mentioned in section V-B.

For the experimental cases, in the first 20 mm of the optical field of view the flame is brighter for lower mixture ratios. After about 20 mm the emission intensity for the mixture ratio 3.4 increases progressively until the end of the optically accessible window. On the other hand, for the numerical cases the OH mass fraction near the faceplate increases with higher mixture ratios.

At about 15 mm, the mass fraction for O/F 2.6 decreases less than the ones of higher mixture ratios. Further downstream the OH mass fractions for the different mixture ratios increase continuosly with a similar rate as the corresponding ones from the experiment.

Due to the fact that the axial profile of the maximum emission intensity does not account for the flame thickness and that in fact the flame is thinner in the numerical simulation than in the experimental results, for future comparison

the authors plan to plot the axial profile of the flame using an interval equivalent to the flame thickness at each axial position. In this way, the relevance of the flame spreading and its thickness will be taken into account in the comparison.

For a more detailed comparison between the experimental and numerical results, the authors also plan to implement the OH^* calculation in the pre-processing step of the Flamelet table calculation. This will be done with the method of Fiala et al. [25] on the results of the laminar counterflow diffusion flames solved in the Flamelet generation step. This way, the turbulent fluctuations will be taken account of by means of the PPDF integration and will not have to be included a posteriori.

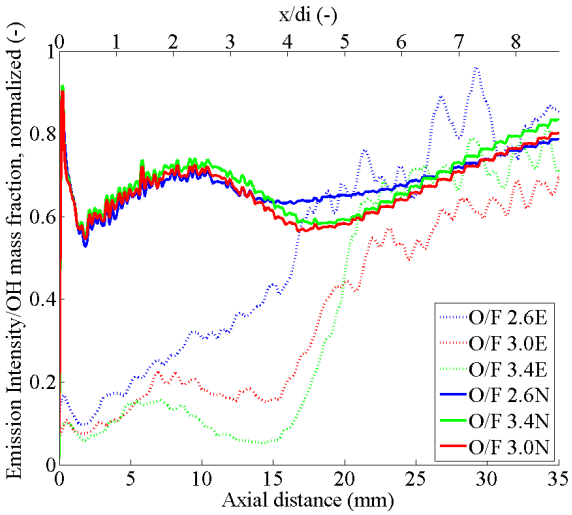

Fig. 16 Comparison between the axial profile of maximum emisson intensity of the experimental results (E) and numerical simulations (N).

VIII. Conclusions

In order to improve the understanding of the former experimental results on thermal behavior and mixing processes of the gaseous methane and oxygen single element shear coaxial injector and to reduce the discrepancies between experimental and numerical results a test campaign using the optical method of emission imaging in addition to the standard measurement techniques as pressure and wall temperature measurements has been performed at 10 and 20 bar pressure level for the mixture ratio of 2.6, 3.0 and 3.4.

The recorded images have been post-processed using image processing techniques. The consecutive instantaneous images were averaged in the phase of stable combustion operation at the evaluation time. The time-averaged OH^* emission images have been de-convoluted using the Abel transformation. The Fourier method is used for the calculation of the de-convolution. This post-processing technique was required in order to compare the experimental results with radiation models.

In this way, the optically accessible combustion chamber allowed for the determination of the flame global shape and characterization of the reaction zone and flame anchoring in the near injector area – information which is relevant not only for the understanding of the inector-wall interaction and experimental heat flux but also for the improvement of numerical tools.

For the comparison with the experimental data, a CFD simulation was carried out. The 3D Reynolds-averaged Navier Stokes equations (RANS) are solved using a finite volume method. The adiabatic Flamelet model described by Peters [20] is implemented in this combustion simulation. For the turbulence model, the standard $k-\epsilon$ was utilized, using a two-layer model by Wolfshtein [22] for the wall treatment.

Experimental and numerical heat flux profiles were compared. The simulation was able to reproduce the heat flux qualitative trend but predicted a higher average. This could be due to experimental evaluation errors as well as the

numerical models used in the simulation. Generally the CFD was capable to capture not only the increasing heat flux level and shift of heat flux maximum towards the exit of the chamber but also the qualitative trend close to the injection plane.

For the present comparison of the OH^* emissions from the experiment with the numerical results the OH mass fraction is selected instead of the OH^* concentration because the method proposed by Fiala et al. when applied to turbulent combustion underpredicts the width of the OH^* zone and hence the flame thickness.

The test results for the mixture ratios 2.6, 3.0 and 3.4 at 20 bar were compared with the numerical simulations. The reacting shear layer between oxygen and methane grows with increasing the axial distance after half of the optically field of view for both, numerical and experimental results. The simulation is able to capture the trend and position of flame expansion.

For future comparison between the experimental and numerical results, the authors plan to further improve the post-processing and data analysis code of the experimental results and to take the turbulent fluctuations into account in the numerical simulations by implementing the OH^* calculation in the pre-processing step of the Flamelet table calculation. In this way, the turbulent fluctuations will not have to be included a posteriori.

Acknowledgments

The authors gratefully acknowledge the financial support provided by the German Research Foundation (Deutsche Forschungsgemeinschaft – DFG) in the framework of the Sonderforschungsbereich Transregio 40 and the Gauss Centre for Supercomputing e.V. (www.gauss-centre.eu) for funding this project by providing computing time on the GCS Supercomputer SuperMUC at Leibniz Supercomputing Centre (www.lrz.de).

References

[1] Haeseler, D.; Bombelli, V.; Vuillermoz, P.; Lo, R.; Marée, T.; Caramelli, F. *Green Propellant Propulsion Concepts for Space Transportation and Technology Development Needs.*. In: 2nd International Conference on Green Propellants for Space Propulsion, Cagliari, Sardinia, Italy, 7 - 8 June 2004.

[2] Vernin, H.; Pempie, P. *LOX/CH4 and LOX/H2 Heavy Launch Vehicle Comparison.* In: 45th AIAA/ASME/SAE/ASEE Joint Propulsion Conference & Exhibit, Denver, Colorado, 2-5 August 2009.

[3] Burkhardt, H.; Sippel, M.; Herbertz, A.; Klevanski, J. *Comparative Study of Kerosene and Methane Propellant Engines for Reusable Liquid Booster Stages.* In: 4th International Conference on Launcher Technology " Space Launcher Liquid Propulsion", Liège, Belgium, 3 - 6 December 2002.

[4] Pempie, P.; Frohlich, T.; Vernin, H. *LOX/Methane and LOX/Kerosene high thrust engine trade-off.* In: 37th AIAA/ASME/SAE/ASEE Joint Propulsion, Salt Lake City, Utah, 8 - 11 July, 2001.

[5] Ueda, S.; Tomita, T.; Onodera, T.; Kano, Y.; Kubota, I.; Munenaga, T. *Hot-firing test of methane-fueled rocket engine under high altitude condition.* In: 49th AIAA/ASME/SAE/ASEE Joint Propulsion Conference & Exhibit, San Jose, California, 14-17 July 2013.

[6] Lux, J.; Suslov, D.; Bechle, M.; Oschwald, M.; Haidn, O. J. *Investigation of sub- and supercritical LOX/Methane injection using optical diagnostics.* In: 42nd AIAA/ASME/SAE/ASEE Joint Propulsion Conference & Exhibit, Sacramento, California, 9 -12 July 2006.

[7] Schuff, R.; Maier, M.; Sindily, O.; Ulrich, C.; Fugger, S. *Integrated modelind and analisys for LOX/Methane expander cycle engine.* In: 42nd AIAA/ASME/SAE/ASEE Joint Propulsion Conference & Exhibit, Sacramento, California, 9 -12 July 2006.

[8] Roth, C.; Haidn, O.; Chemnitz, A.; Sattelmayer, T. *Numerical Investigation of Flow and Combustion in a Single-Element GCh4/GOX Rocket Combustor.* In: 52nd AIAA/SAE/ASEE Joint Propulsion Conference, Salt Lake City, UT, 25 - 27 June 2016.

[9] Celano, M. P.; Silvestri, S.; Pauw, J.; Perakis, N.; Schily, F.; Suslov, D.; Haidn, O. J. *Heat Flux Evaluation Methods for a Single Element Heat-Sink Chamber.* In 6th European Conference for Aerospace Sciences, Kraków, Poland, 29 June - 3 July 2015.

[10] Silvestri, S.; Celano, M. P.; Schlieben, G.; Haidn, O. J. *Characterization of a Multi-Injector GOX-GCH4 Combustion Chamber.* In 52nd AIAA/SAE/ASEE Joint Propulsion Conference, Salt Lake City, UT, 25 - 27 June 2016.

[11] Celano, M. P.; Silvestri, S.; Schlieben, G.; Kirchberger, C.; Haidn, O. *Injector Characterization for a GOX-GCH4 Single Element Combustion Chamber.* In: 5th European Conference for Aeronautics and Space Sciences, Munich, Germany, 1 - 5 July 2013.

[12] Bauer, C. ; Schlieben, G. ; Eiringhaus, D. ; Haidn, O. *Design and commission of a mobile GOX/GCH4 rocket combustion test bed for education and collegiate research.* In : Joint Conference 29th ISTS, 24th ISSFD & 6th NSAT, Japan, 2013.

[13] Pretzier, G. *A new method for numerical Abel-inversion.* Zeitschrift für Naturforschung, A 46, n. 7, 1991, p. 639-641.

[14] Behrens, A. A.; Lutz, J. M.; Strykowsky, P. J. *Instantaneous Flame Anchor Measurements behind a Bluff Body.* In: 19th Propulsion Conference, Costa Mesa, CA, December 2006.

[15] Behrens, A. A.; Lutz, J. M.; Strykowsky, P. J. *Instantaneous Flame Anchor Measurements behind a Rearward-Facing Step.* AIAA Journal, v.47, n. 6, June 2009.

[16] Frolov, S. M.; Basevich, V. Ya.; Belyaev, A. A. *Mechanism of Turbulent Flame Stabilization on a Bluff Body.* Chem. Phys. Reports, v. 18(8), p. 1495-1516, 2000.

[17] Fluent, A. *"Ansys fluent theory guide," ANSYS Inc.* USA, Vol. 15317, 2011, pp. 724–746.

[18] Celano, M. P., Silvestri, S., Pauw, J., Perakis, N., Schily, F., Suslov, D., and Haidn, O. J. *Heat Flux Evaluation Methods for a Single Element Heat-Sink Chamber.* In: 6th European Conference for Aerospace Sciences (EUCASS), Krakow, 2015.

[19] Perakis, N., Celano, M. P., and Haidn, O. J. *Heat flux and temperature evaluation in a rectangular multi-element GOX/GCH4 combustion chamber using an inverse heat conduction method.* In: 7th European Conference for Aerospace Sciences (EUCASS), Milano, 2017.

[20] Peters, N. *Laminar diffusion flamelet models in non-premixed turbulent combustion.* Progress in energy and combustion science, Vol. 10, No. 3, 1984, pp. 319–339.

[21] Slavinskaya, N., Abbasi, M., Starcke, J.-H., Mirzayeva, A., and Haidn, O. J. *Skeletal Mechanism of the Methane Oxidation for Space Propulsion Applications.* in: 52nd AIAA/SAE/ASEE Joint Propulsion Conference, 2016, p. 4781.

[22] Wolfshtein, M. *he velocity and temperature distribution in one-dimensional flow with turbulence augmentation and pressure gradient.* International Journal of Heat and Mass Transfer, Vol. 12, No. 3, 1969, pp. 301–318.

[23] Perakis, N., Rahn, D., Eiringhaus, D., and Haidn, O. J. *Heat transfer and combustion simulation of a 7-element GOX/GCH4 rocket combustor.* Joint Propulsion Conference, Cinncinati, 2018.

[24] Bird, R. B., Stewart, W. E., and Lightfoot, E. N. *Transport phenomena.* Madison, USA, 1960.

[25] Fiala, T., and Sattelmayer, T. *A Posteriori Computation of OH* Radiation from Numerical Simulations in Rocket Combustion Chambers.* In: 5th European Conference for Aerospace Sciences (EUCASS), Munich, 2013.

Annex

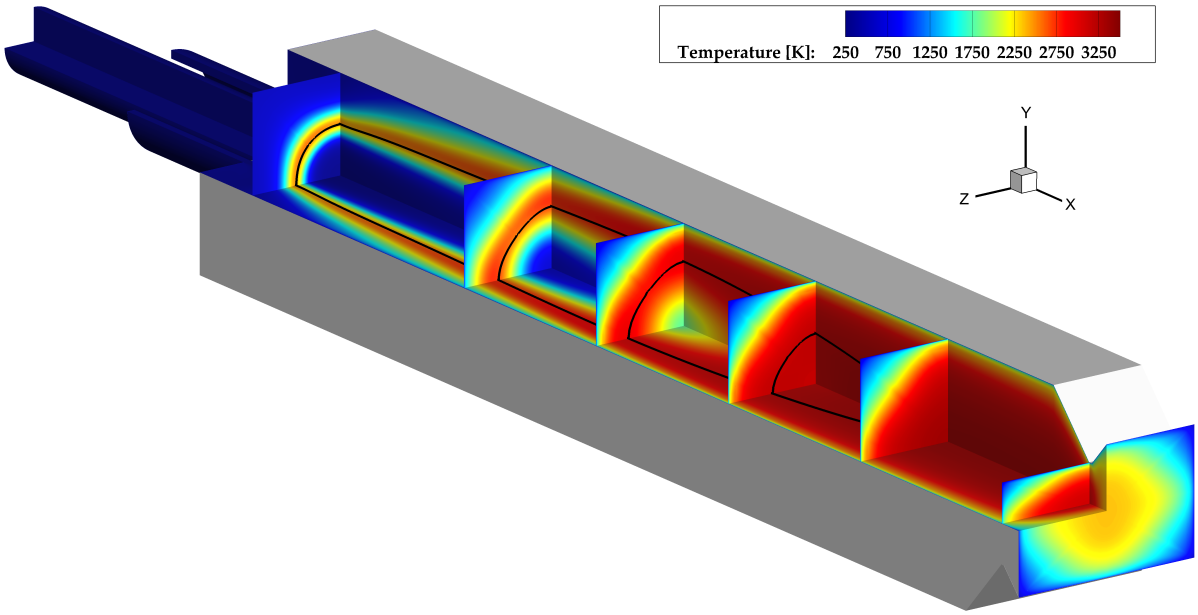

(a) O/F 2.2

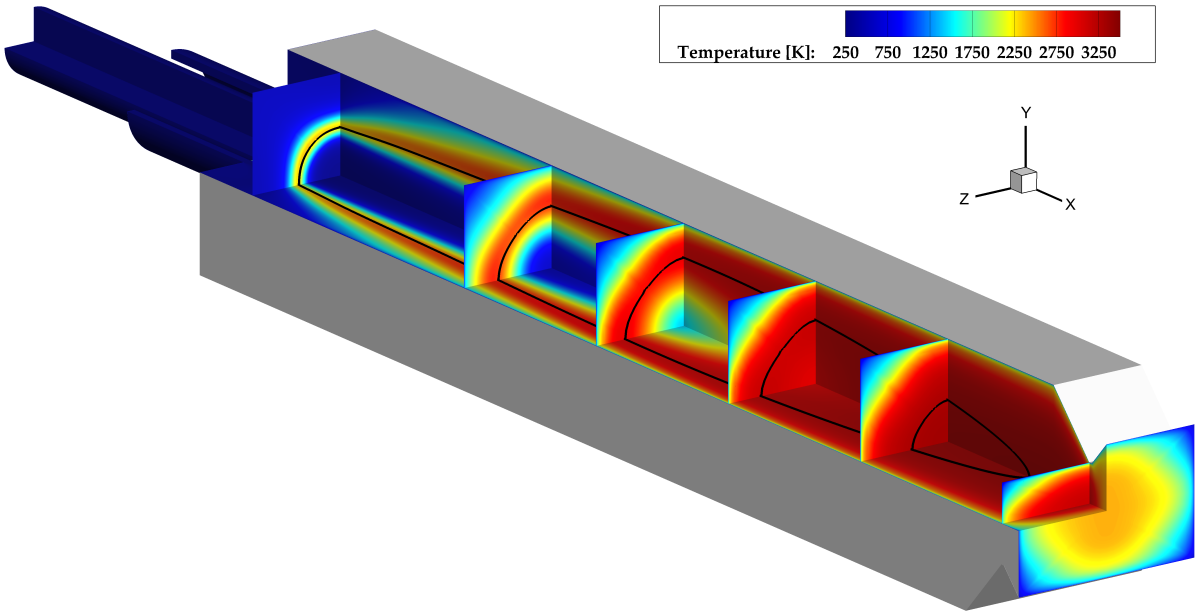

(b) O/F 2.6

Fig. 17 Temperature field for the O/F cases 2.2 and 2.6 at 20 bar pressure. The solid black line shows the stoichiometric concentration.

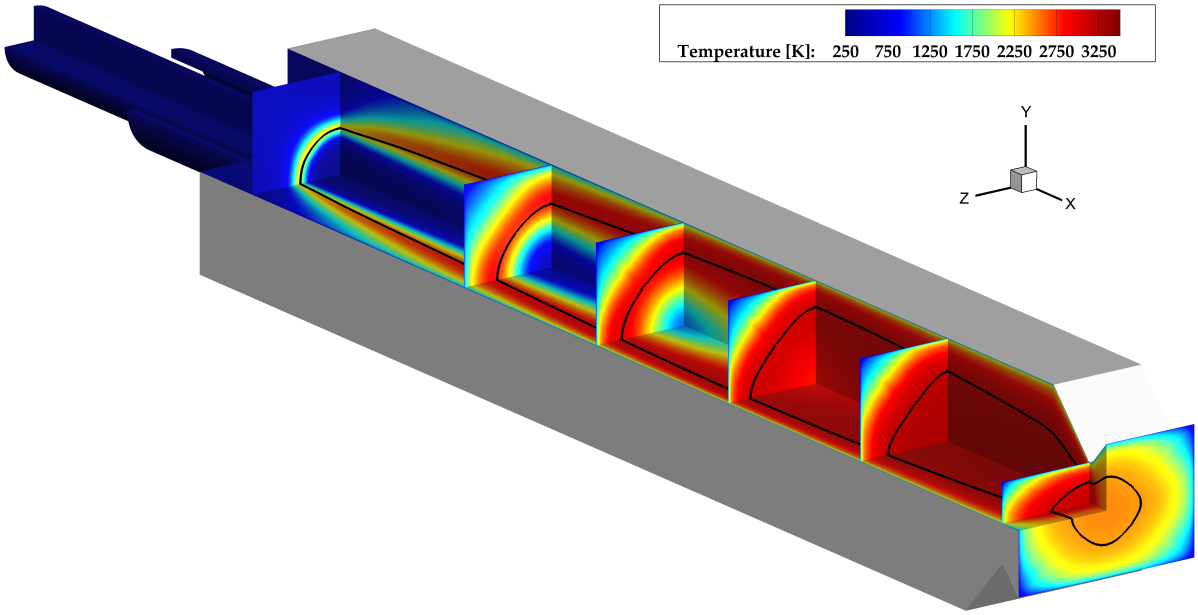

(a) O/F 3.0

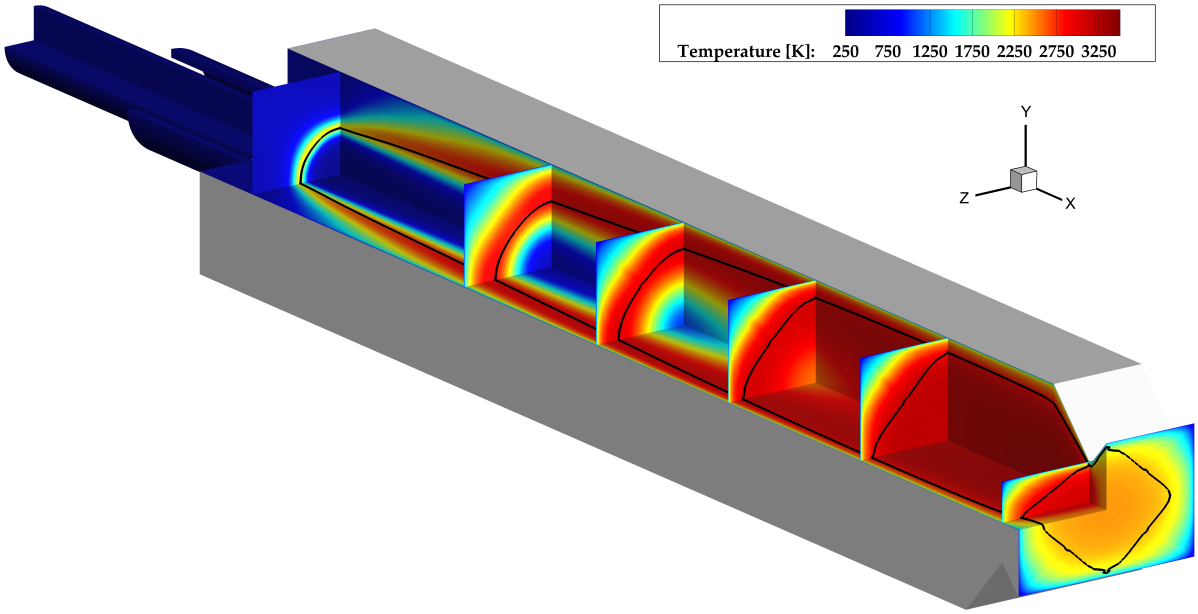

(b) O/F 3.4

Fig. 18 Temperature field for the O/F cases 3.0 and 3.4 at 20 bar pressure. The solid black line shows the stoichiometric concentration.